Nanoscale coupling of MoS_2 and graphene via rapid thermal decomposition of ammonium tetrathiomolybdate and graphite oxide for boosting capacity of Li-ion batteries

V. O. Koroteev[a], S. G. Stolyarova[b], A. A. Kotsun[b], E. Modin[a], A. A. Makarova[c], Yu. V. Shubin[b], P. E. Plyusnin[b], A. V. Okotrub[b], L. G. Bulusheva[b,1]

[a]*CIC nanoGUNE BRTA, Tolosa Hiribidea 76, E-20018 Donostia - San Sebastian, Spain*

[b]*Nikolaev Institute of Inorganic Chemistry SB RAS, 3 Acad. Lavrentiev Ave., 630090 Novosibirsk, Russia*

[c]*Physikalische Chemie, Institut für Chemie und Biochemie, Freie Universität Berlin, 14195 Berlin, Germany*

Abstract. We report the MoS_2/graphene coupling as the result of the decomposition of a mixture of ammonium tetrathiomolybdate and graphene oxide in thermal shock conditions. X-ray diffraction and Raman spectroscopy showed that the temperature of 400°C is sufficient for the formation of MoS_2 crystallites. High-resolution electron microscopy detected that nanoscale MoS_2 crystallites are oriented along or perpendicular to the graphene surface or they are incorporated between the graphene layers. Electron energy loss C K-edge spectra confirmed a firm bonding between the components. Used as the electrodes of Li-ion batteries, the materials were able to sustain a specific capacity of 564 $mAhg^{-1}$ at a current density of 10 Ag^{-1} with gradual growth of the capacity up to ~1730 $mAhg^{-1}$ during next 425 operation cycles at 0.1 Ag^{-1}. Our study revealed that rapid decomposition of the precursors creates defects in the graphene and MoS_2 layers, short synthesis time enables the formation of few-layer MoS_2 nanosheets, and high pressure, developed in the reactor, leads to covalent bonding between the components. These structural features ensure many sites for the adsorption of Li ions, fast transport of the ions, and high stability of the electrode during long-term operation of the battery.

Keywords: graphene; molybdenum disulfide; thermal shock; nanoscale coupling; Li-ion battery

[1]corresponding author, e-mail: bul@niic.nsc.ru

1. Introduction

Hexagonal MoS_2 is a semiconducting material with a distance of 0.62 nm between the three-atomic S-Mo-S layers [1]. Its electrochemical interaction with lithium ions includes the intercalation of lithium into the interlayer space and the conversion of Li_xMoS_2 intercalates to molybdenum and Li_2S [2]. The intercalation and conversion processes yield to specific capacities of 167 and 502 mAh g^{-1}, respectively. Studies of MoS_2-based electrodes have shown that the extraction of lithium ions results in the formation of sulfur species [3]. In the following charge-discharge cycles, the battery works like the Li–S system, where the redox reaction of elemental sulfur with lithium yields a theoretical capacity of 1675 mAh g^{-1} [4]. Dissolution of intermediate polysulfides in the electrolyte results in fading of the capacity and addition of carbon in the electrode material prevents this process [5]. Graphitic carbon component stabilizes the active material and improves its electrical conductivity [6].

Chang K. and Chen W. were the first to propose a method of the synthesis of nanostructured MoS_2/graphene materials by a hydrothermal treatment of sodium molybdate and graphene oxide (GO) in the presence of an organic compound [7, 8]. The materials were able to deliver the specific capacity of 1187–1290 mAh g^{-1} at a current density of 0.1 A g^{-1} with no capacity fading during 50–100 cycles of the Li-ion battery operation. To date, several approaches are proposed to obtain MoS_2/graphene nanomaterials and their description can be found in a recent review [9]. The synthesis may include hydrothermal [10, 11], solvothermal [12, 13], sonication [14], microwave [15], and hot pressing [16, 17] treatments or be based on self-assembly [18, 19] and template [20] methods. The best reversible capacities for the MoS_2/graphene anodes tested in Li-ion batteries at a current density of 0.1 A g^{-1} are within the range of 1350–1390 mAh g^{-1} [14, 21–24]. An even higher value of 1670 mAh g^{-1} is reported for MoS_2 layers vertically grown on mesoporous carbon [25]. These high specific capacities cannot be explained by exclusively redox reactions between sulfur and lithium because the weight of the working electrode accounts molybdenum, which is inactive in these reactions. One of the reasons for the boost of the Li storage could be the augmentation of the surface and interfacial area in nanostructured electrodes that leads to more active sites for the adsorption of Li ions [26]. Reducing the anode materials to nanoscale can also prevent large volume changes during cycling and thus extend battery life [27].

Many various architectures were designed to achieve the highest synergism between carbon and MoS_2 components and improve the performance of the composite material in Li-ion batteries. It was shown that the vertical orientation of MoS_2 sheets relative to the graphene surface and enlarged distance between the sheets increase the rate capability of the battery [25, 28–31]. A high crystallization of MoS_2 and graphene layers and tight interface contact between their basal planes decreases the loss of the capacity at the first insertion of Li ions [32]. Sandwiching of MoS_2

between graphene layers [33–35] and encapsulation of MoS_2 in graphene-like spheres [24, 36], or carbon matrixes [37, 38] prevent fading of the capacity during long-term cycling at high current densities.

The studies of electrode materials after several discharge-charge cycles detected Mo clusters with a size smaller than 2 nm [39–41]. The calculations performed within density functional theory (DFT) predict that these clusters readily interact with lithium [41]. Hence, the reversible formation of Mo_xLi_y species can contribute to the lithium storage in MoS_2-based electrodes [42]. The Mo clusters could also act as pining sites for lithium polysulfides thus preventing their dissolution [43]. Stabilization of atoms or clusters of molybdenum can be achieved through the bonding with functional groups [44–46] or dangling carbon atoms [47, 48] present in the structure of carbon component. A strong interaction at the MoS_2/graphene interface boosted the charge transfer [44] and contributed to the steady growth of the capacity [48].

In this paper, we report a simple approach, based on simultaneous thermal decomposition of the precursors of MoS_2 and graphene in an inert atmosphere, which provides a tight coupling of the components at nanoscale. This technique has shown a capability for the preparation of few-layer graphene materials from the graphite derivatives [49]. Here, the mixtures of graphene oxide (GO) and ammonium tetrathiomolybdate (ATM), $(NH_4)_2MoS_4$, are used to obtain few-layer MoS_2 nanocrystals distributed on the graphene surface or between the graphene layers. Electrochemical tests of the MoS_2/graphene materials showed superior performance in Li-ion batteries.

2. Experimental

2.1 Materials

Graphite oxide was synthesized using a modified Hummer's method. The details of the synthesis and results of characterization of the product are described elsewhere [50]. ATM was prepared by passing gaseous H_2S through an ammonium solution of $(NH_4)_6Mo_7O_{24}\cdot 4H_2O$. Needle reddish-brown crystals were collected on a glass filter, washed with ethanol, and dried in air.

The weighted graphite oxide specimen was dispersed in water using mechanical stirring and a certain amount of freshly prepared ATM was added there. After the complete dissolution of ATM, the container with the suspension was immersed into liquid nitrogen. The obtained product was freeze-dried under 10 Pa at –50 °C to get ATM/GO aerogel. A vertical quartz reactor constantly flushed with argon was heated by an electrical oven to 400 °C and the aerogel was quickly placed there. After 15 s, the reactor was removed from the oven and naturally cooled to room temperature. The ratio of the precursors used in the synthesis was calculated according to the decomposition reaction of ATM $(NH_4)_2MoS_4 \rightarrow MoS_2 + 2NH_3\uparrow + 2H_2S\uparrow$, and considering~45% weight loss of used GO under thermolysis at 400 °C (Fig. S1). The masses of the ATM and graphite oxide were

in a ratio of 0.81, 1.62, and 2.44 to obtain MoS_2/graphene materials with the corresponding weight ratio of the components 1:1, 2:1, and 3:1, respectively. These samples are denoted as 1MoS_2/G, 2MoS_2/G, and 3MoS_2/G, respectively. Reference samples were synthesized from pure ATM (MoS_2 sample) and pure GO (G sample) under the same synthesis conditions as hybrid samples.

2.2 Instrumental methods

Thermogravimetric (TG) study of GO and ATM/GO aerogels was performed on an STA 449 F1 Jupiter thermal analyzer in a helium flow (30 mL min^{-1}) at a heating rate of 10 °C min^{-1}. The study was accompanied by evolved gas analysis (EGA) using a QMS 403D Aëolos quadrupole mass spectrometer (MS, Netzsch, Germany). An electron impact ionizer operated at an energy of 70 eV. Ion currents of the selected mass/charge (m/z) numbers were monitored in multiple ion detection mode with a collection time of 1 s for each channel.

Contents of elements in MoS_2/G samples were determined using a vario MICRO cube analyzer (Elementar, Germany) in the CHNS mode. The specific surface area of the samples was calculated by the Brunner-Emmett-Teller (BET) method using N_2 adsorption/desorption isotherms recorded on a Sorbi-MS analyzer (ZAO "Meta", Russia) at 77 K.

Morphology and structure of MoS_2/G samples were characterized by scanning electron microscopy (SEM) on a FEI Helios 450S dual-beam microscope and high-resolution transmission electron microscopy (HR TEM) on a Titan 60-300 microscope (FEI, The Netherlands) using 80 kV acceleration voltage. Electron energy loss (EEL) C K-edge spectra were recorded using a high resolution Quantum GIF spectrometer (Gatan, USA). A specimen was prepared by ultrasonic dispersion of MoS_2/G in isopropanol on a copper TEM grid.

The phases were identified using X-ray diffraction (XRD) patterns taken on a Shimadzu XRD-7000 diffractometer (Cu Kα radiation, Ni filter on the reflected beam). Raman scattering was recorded with a Spex triple spectrometer using an Ar^+ laser at 488 nm. The power and spot of the laser beam were 0.5 W mm^{-2} and 0.1 mm, respectively.

X-ray photoelectron spectroscopy (XPS) experiments were performed at the Berliner Elektronenspeicherring für Synchrotronstrahlung (BESSY II), Helmholtz Zentrum Berlin using radiation from the Russian–German beamline. The spectra were measured using monochromatized radiation at 830 eV with an energy resolution of better than 0.4 eV (full width at half maximum, FWHM).

2.3 Electrochemical measurements

The working electrodes were prepared by mixing the material used (80 wt.%), super P (10 wt.%) and polyvinylidene fluoride (10 wt.%) in N-methyl-2-pyrrolidinone (NMP). The resulting suspension was distributed over a copper foil and dried at 60 °C for 12 h under vacuum. The weight

of each electrode material was *ca.* 1 mg. The CR2032 coin cells were assembled in a glove box filled with argon, with lithium metal as the counter electrode. The electrolyte was a 1 M solution of $LiPF_6$ in a mixture of ethylene carbonate and dimethyl carbonate (1: 1 by volume) from Merck Co. Galvanostatic charge/discharge tests were performed on a NEWARE CT-3008 station in the voltage range from 0.01 to 2.50 V vs. Li/Li^+ at current densities from 0.1 A g^{-1} to 10 A g^{-1}. Cyclic voltammograms (CV) were recorded using a Bio-Logic SP-300 station from 0.01 to 3.0 V.

3. Results and discussion

The summary of MoS_2/G materials preparation is shown in Fig. 1. GO strongly interacts with H_2O molecules via oxygen-containing groups, resulting in its delamination and the formation of stable aqueous suspension [51]. In this suspension, the surface of the layers is highly assessable for ATM molecules. We expect that fast freezing of the solution to the temperature of liquid nitrogen and removal of the ice by sublimation produce an aerogel consisting of GO layers uniformly coated by ATM species. Thermal decomposition of the aerogel accompanied by flushing of the reactor with an inert gas should yield MoS_2 nanocrystals anchored to the surface of graphene.

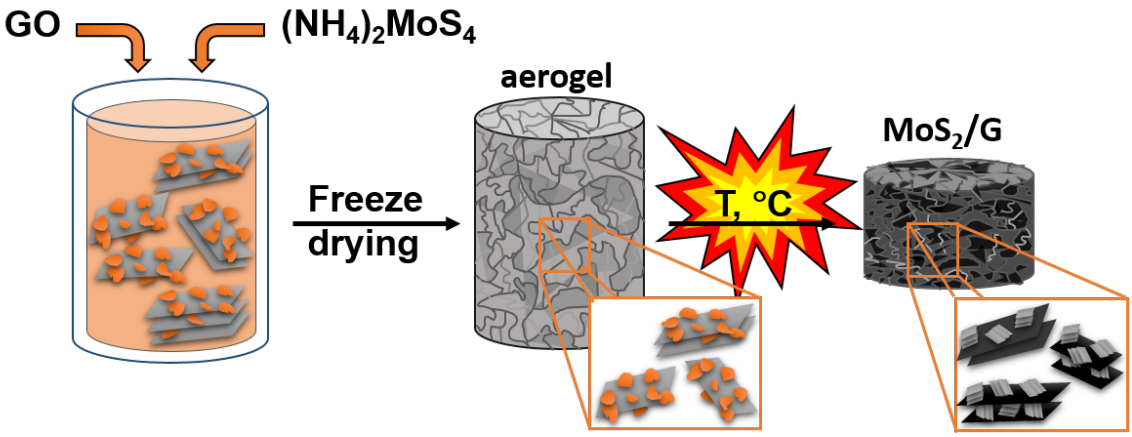

Figure 1. Schematic presentation of the process of the synthesis of MoS_2/graphene samples.

TG study of the decomposition of ATM/GO aerogel in helium atmosphere revealed three stages (Fig. S2): GO loses oxygen groups between 110 and 210 °C, $(NH_4)_2MoS_4$ decomposes to MoS_3 at about 310 °C, and MoS_3 decomposes to MoS_2 at about 410°C. These values agree with the characteristic temperatures of GO reduction and thermal transformation of ATM from the literature [52–54]. The aerogel continues to lose weight up to 800 °C (Fig. S2). The main released gas in the temperature range of 410–750 °C is CO_2, which indicates continuous GO decomposition.

To obtain the MoS_2 crystals as small as possible, the syntheses of the MoS_2/graphene materials were carried out at 400 °C. Concentrations of elements determined from the CHNS analysis are summarized in Table 1. Note, that the samples contain traces of nitrogen derived from ATM. The

concentration of carbon is systematically lower than that assumed from the ATM and GO decomposition reactions. Under thermal shock conditions some carbon atoms from graphene lattice are removed together with oxygen atoms. This process is favorable when the hydroxyl and epoxy groups are located near to each other [55]. However, the fraction of carbon in the samples is in correlation to the ratio of precursors, used for sample preparation. A decrease in the amount of carbon in a set of samples $1MoS_2/G>2MoS_2/G>3MoS_2/G$ is accompanied by a reduction of the BET surface area from *ca.* 57 m^2 g^{-1} determined for $1MoS_2/G$ to *ca.* 6 m^2 g^{-1} for $2MoS_2/G$ and then to *ca.* 5 m^2 g^{-1} for $3MoS_2/G$. The concentration of sulfur in the products also changes in accordance with the ratio of ATM and GO used in the synthesis and the CHNS values well agree with the expected ones. The total content of molybdenum and oxygen, which was determined as the residual weight of the analyzed sample, is almost constant and this may indicate an excess of sulfur in $2MoS_2/G$ and $3MoS_2/G$ at least. According to the XPS data, all samples are enriched by sulfur (Table 1) as compared to ideal MoS_2 composition and the sulfur to molybdenum ratio increases with the use of more ATM in the synthesis. The concentrations of elements determined by the two methods are in fairly good agreement and the differences may be due to the fact that XPS is a surface-sensitive method.

Table 1. Concentrations of elements in MoS_2/G materials expected from decomposition reactions of ATM and GO and determined by CHNS (error ~10%) and XPS (error ~10%) analyzes.

Sample	Expected, wt%			CHNS, wt%				XPS, wt%			
	C	S	Mo	C	S	N	Mo+O	C	S	Mo	O
$1MoS_2/G$	50	20	30	33.3	22.6	1.8	42.3	45.1	18.8	22.5	13.5
$2MoS_2/G$	33	27	40	22.9	31.1	1.5	44.5	43.7	20.2	20.4	15.8
$3MoS_2/G$	25	30	45	15.9	39.5	1.2	43.4	30.6	28.2	23.6	17.6

SEM study of the synthesized materials showed interconnected thin graphene layers (Fig. 2). The image of $1MoS_2/G$ sample (Fig. 2a) is typical for aerogels and hydrogels prepared from reduced GO [18, 56]. An increase in the loading of graphene layers by MoS_2 causes the formation of denser structures (Fig. 2b,c). The same regions of the samples recorded in back-scattering electron (BSE) mode are shown in Fig. 2d–f. Since molybdenum and sulfur are heavier than carbon, they provide more backscattered electrons and appear on the image as bright regions. Uniform BSE contrast of the most graphene layers implies homogeneous distribution of MoS_2 layers in the $1MoS_2$/graphene materials. Bright dendritic structures observed in $2MoS_2/G$ and $3MoS_2/G$ samples (Fig. 2e, f) correspond to MoS_2 crystals trapped between thin graphene layers. Previously, the growth of the dendritic MoS_2 monolayers was observed in chemical vapor

deposition syntheses when the relative concentration of sulfur was large [57]. This is also true for our syntheses, carried out at the temperature, when according to the TG data excess sulfur is still not removed from the decomposition products (Fig. S2).

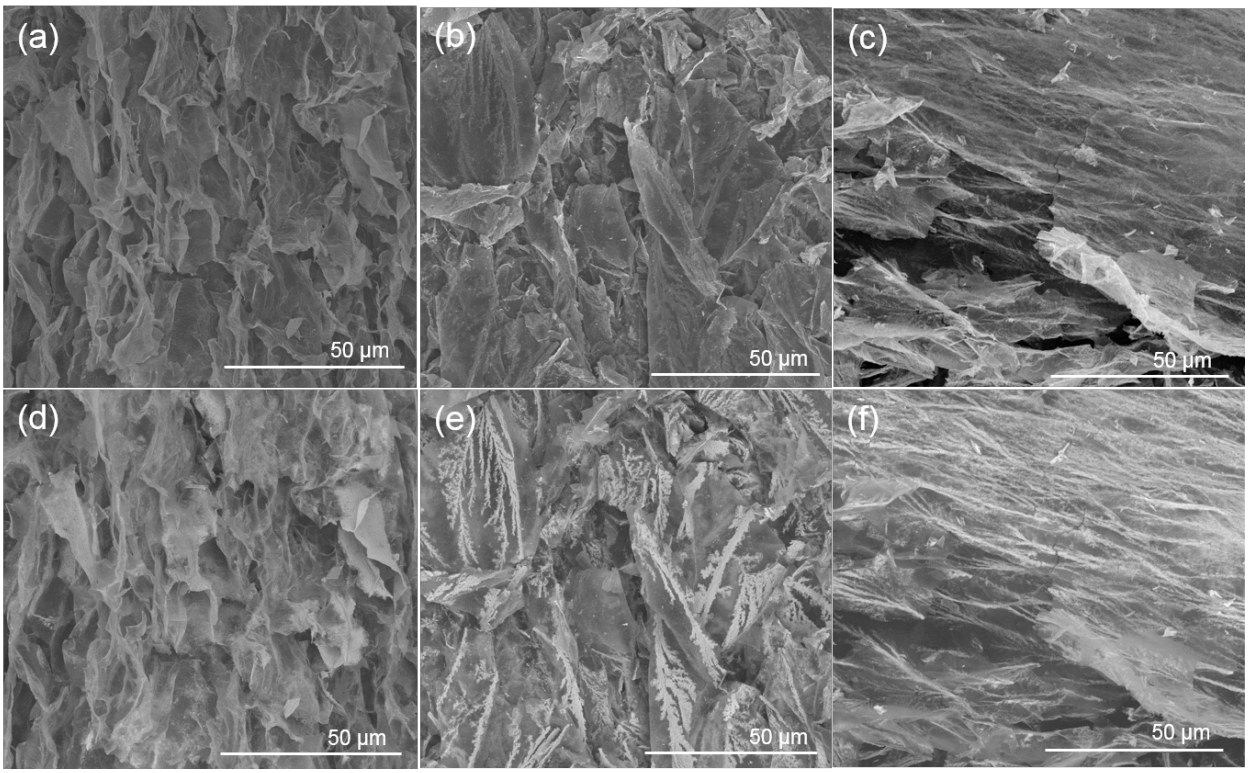

Figure 2. SEM images of $1MoS_2/G$ (a, d) $2MoS_2/G$ (b, e) and $3MoS_2/G$ (c ,f) in conventional mode (a–c) and BSE mode (d–f).

A comparison of the XRD patterns demonstrated a decrease in the relative intensity of (002) graphitic reflection with an increase of the MoS_2 fraction in the obtained materials (Fig. 3a). Due to a complex shape of the patterns, the width of this reflection is hard to determine, however, the absence of a sharp peak at the corresponding diffraction position is a sign of high exfoliation ratio of the graphene layers. The peak at about $2\theta=14.4°$ corresponds to the distance of 0.62 nm, characteristics of the interlayer spacing in 2H-MoS_2 [58]. This peak is suppressed in the pattern of $1MoS_2/G$ as compared to the samples with higher MoS_2 loading. Since the XRD data were collected for samples of approximately the same mass and under identical experimental conditions, the lower intensity of the (002) 2H-MoS_2 reflection indicates a smaller number of stacked layers in $1MoS_2/G$. This number is most likely less than five [59]. The presence of (*hkl*) reflections at *ca.* 33.5, 40.1, and 58.9° in the patterns of all samples characterizes atomic ordering in the MoS_2 layers.

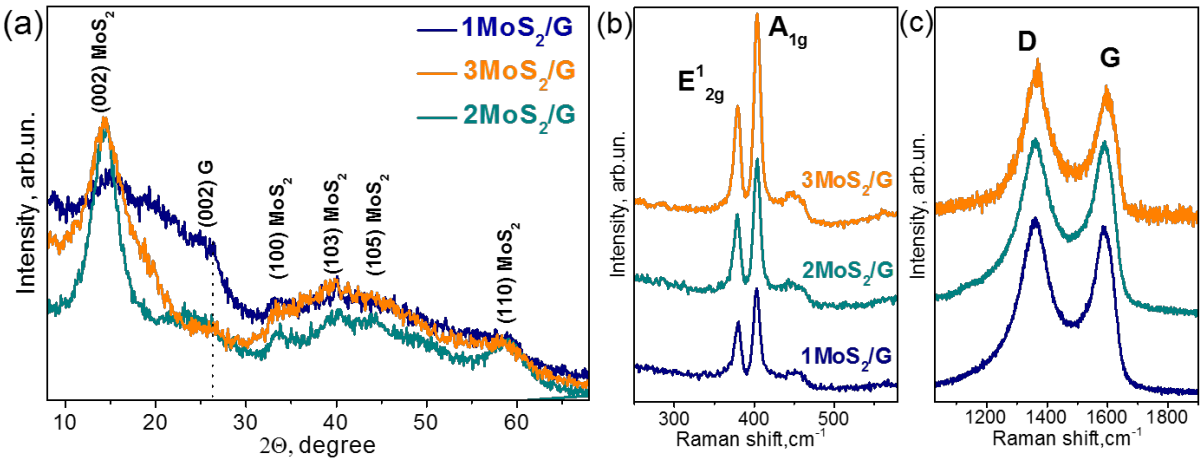

Figure 3. XRD pattern (a) and Raman scattering of MoS_2 component (b) and graphene component (c) measured for synthesized samples.

Raman spectroscopy confirmed the formation of MoS_2 in all the studied samples (Fig. 3b). Positions of peaks E^1_{2g} and A_{1g} associated with in-plane and out-of-plane vibrations of atoms in the MoS_2 layers are 379.3–380.1 cm^{-1} and 403.2–403.9 cm^{-1}, respectively. These values, while being significantly smaller than the corresponding values of 383 and 408 cm^{-1} for bulk MoS_2 [60], could not be explained by any form of MoS_2 few-layer structures [61]. The softening of intralayer MoS_2 vibrations is attributed to strong coupling with the support and strain in the layers [62]. The number of layers affects the distance between peaks E^1_{2g} and A_{1g}. This value is *ca.* 24.3 cm^{-1} for $2MoS_2$/G and $3MoS_2$/G samples and it decreases to *ca.* 23.1 cm^{-1} for $1MoS_2$/G. Based on the reference data for MoS_2 flakes [61], we conclude the number of stacked MoS_2 layers in the first two samples is about 5–6 and about 3 in the latter sample. In the interval from 1000 to 2000 cm^{-1} the spectra exhibited peaks corresponding to the carbon component in the samples (Fig. 2c). G-peak located at 1591 cm^{-1} originates from the stretching of C-C bonds and D-peak at 1359 cm^{-1} is induced by disorder in sp^2-hybridized carbon lattice [63]. High relative intensity of D-peak is common for graphene materials obtained by the thermal expansion of graphite oxide [64]. Folds, atomic vacancies, topological defects, and sp^3-bonds with the residual hydrogen and oxygen are responsible for D-peak activation.

The electronic state of carbon, sulfur, and molybdenum was analyzed for $2MoS_2$/G. C 1s spectrum of the sample exhibited a dominant peak at *ca.* 284.6 eV (Fig. 4a), which is characteristic of sp^2-hybridized carbon. A component at *ca.* 285.3 eV is attributed to disordered sp^2-carbon surfaces including possibly C–H bonds [65]. The C–S bonding between graphene and MoS_2 in the hybrid gives the component at *ca.* 286.1 eV [66, 67]. The C–O component at *ca.* 287 eV can be attributed to carbon interacting with hydroxyl group or to C–O–Mo bonding. Weak components at *ca.*288.1 and 289.2 eV correspond to carbonyl and carboxyl groups, respectively. The fitting of

the spectrum that *ca.* 10 % of carbon is bound to oxygen. TG-EGA data for ATM/GO aerogel recorded a high ion current corresponding to CO_2 at a temperature of *ca.* 600°C (Fig. S2), since our samples produced at 400°C contain a small fraction of carbon bonded with oxygen, we conclude that decomposition of GO under thermal shock occurs much faster than that with slow heating.

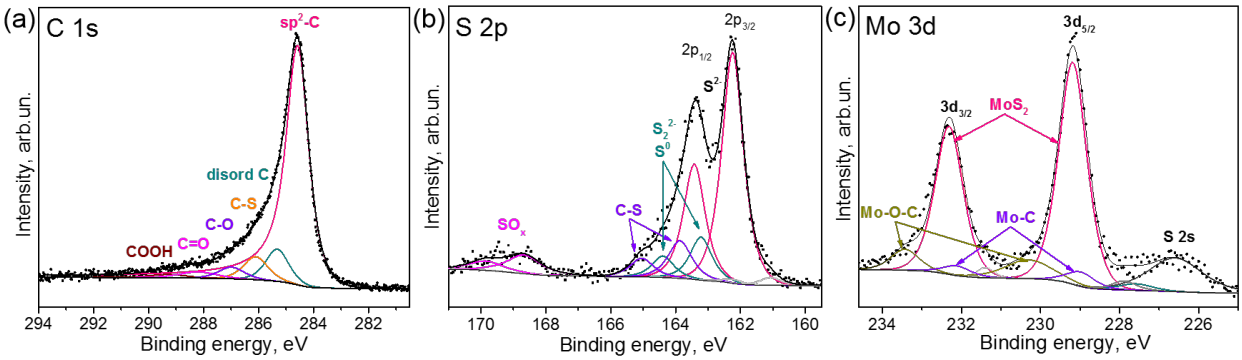

Figure 4. XPS C 1s (a), S 2p (b), and Mo 3d (c) spectra of $2MoS_2$/G sample.

The XPS S 2p spectrum of $2MoS_2$/G was fitted by $2p_{3/2}/2p_{1/2}$ spin-orbit doublets with the intensity ratio of 2:1 of the components and the splitting of 1.2 eV (Fig. 4b). An intense doublet with binding energies of the $2p_{3/2}/2p_{1/2}$ components of 162.2/163.4 eV corresponds to sulfide S^{2-} in MoS_2 [68]. Next doublet at 163.2/164.4 eV is attributed to bridging S_2^{2-} pairs at the edges of MoS_2 layers [54] or elemental sulfur S^0 [69]. A doublet at 163.9/165.1 eV could be assigned to S–C bonds [67, 70] at the MoS_2/graphene interface. A low-energy shoulder is due to the MoS_2 edge-like sites [71]. The high-energy doublet indicates the presence of oxidized sulfur states on the sample surface [69]. Non-oxidized sulfur states form a low-energy S 2s peak in the region of Mo 3d core levels (Fig. 4c). The XPS Mo 3d spectrum of $2MoS_2$/G was fitted by three spin-orbit doublets with the intensity ratio of 3:2 for the $3d_{5/2}/3d_{3/2}$ components separated by ~3.1 eV. The dominant doublet at 229.2/232.3 eV corresponds to the Mo^{4+} state in MoS_2 [68], the weak doublet at 229.0/232.1 eV is attributed to tight Mo–C contacts [72] and component Mo–O–C at 230.3/233.4 eV is assigned to the bonding between graphene and MoS_2 through oxygen. [17].

A firm bonding between graphene and MoS_2 layers achieving in thermal shock conditions was also confirmed using EELS measurements for graphene areas rarely populated by MoS_2 nanoparticles and completely covered by MoS_2 (Fig. 5a,b). The C K-edge spectra (Fig.5c) for both areas exhibited the π* and σ* resonances characteristic of sp^2-hybridized carbon materials [73]. The spectrum of graphene under continuous MoS_2 coating shows an increase in the intensity between these resonances, which is commonly attributed to covalent bonds of carbon atoms with foreign elements. In our case, these spectral features could indicate the formation of C–S, C–Mo–S, or C–O–Mo bonds between graphene and MoS_2. These bonds were identified in the XPS spectra

(Fig. 4). It has been shown that covalent bonds between MoS_2 and carbon component enhance the stability of electrode materials in Li-ion batteries [46, 48, 70, 74, 75].

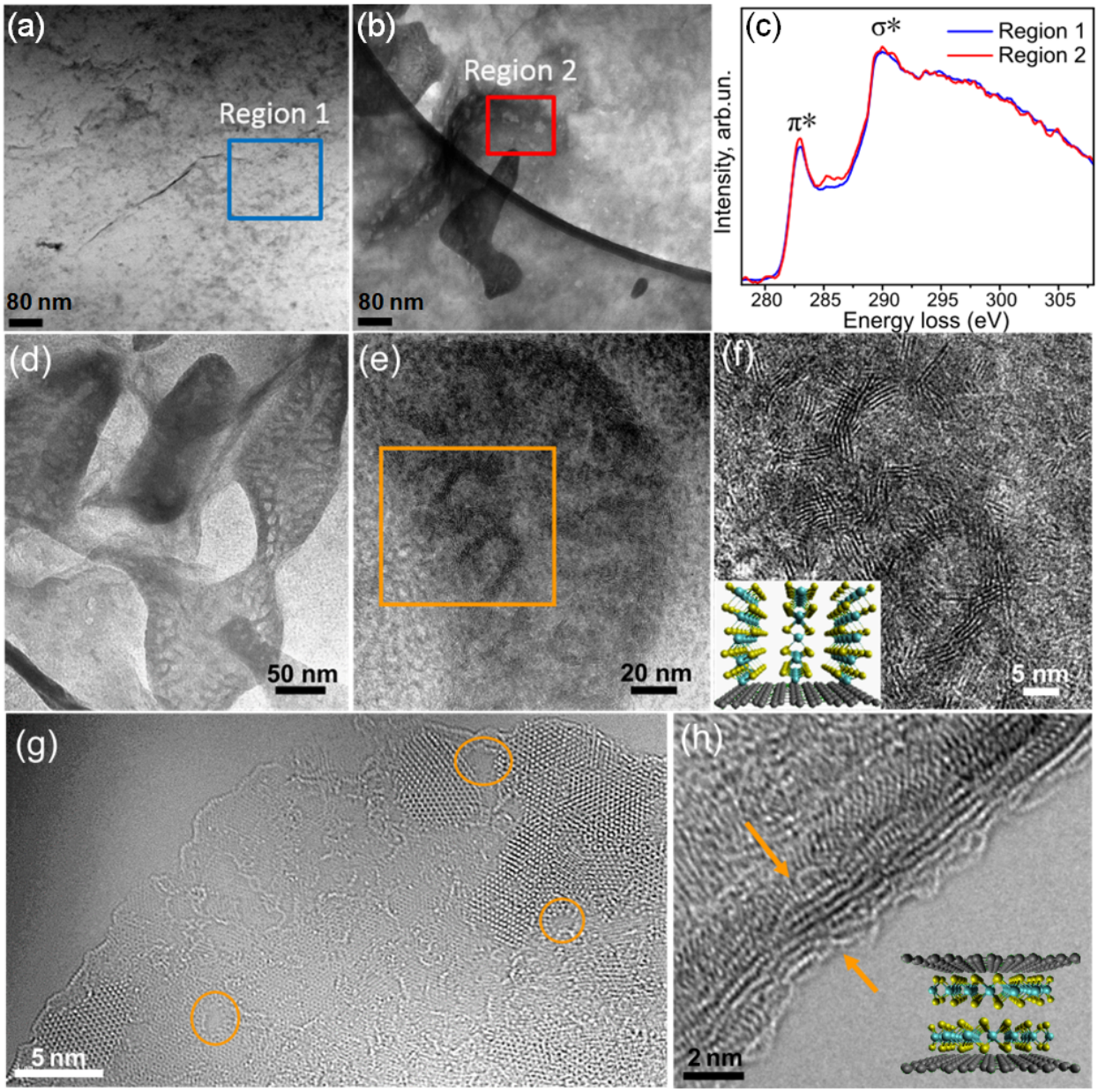

Figure 5. TEM images of $2MoS_2$/G sample (a,b) and EEL spectra measured at C K-edge (c) for the selected regions. TEM images of $2MoS_2$/G sample showing (d) porous deposits on graphene layers, (e) MoS_2 agglomerates in deposit, (f) intertwined MoS_2 nanosheets vertically oriented to graphene surface (enlarged squire from (e)) and MoS_2 layers aligned along graphene surface (g) and sandwiched between defective graphene layers (h). Nanoscale vacancy defects in graphene layers are shown by circles in (g).

TEM study detected porous deposits on or between graphene layered (Fig. 5d). HR TEM images showed that the deposits consist of vertically oriented MoS_2 nanosheets (Figs. 5e,f). The intertwining of nanosheets from neighboring stacks produces pores. MoS_2 monolayers and bi-

layers are distributed along with the graphene layers on the surface of flakes (Fig. 5g) or forming the sandwich-like structure (Fig. 5h). Decomposition of GO in thermal shock conditions results in the formation of nanoscale pores in graphene layers (shown by circles in Fig. 5g).

Electrochemical tests of the synthesized materials in Li-ion half-cells detected initial values of the specific capacity equal to 1150 mAh g^{-1} for $1MoS_2/G$, 1640 mAh g^{-1} for $2MoS_2/G$, and 1213 mAh g^{-1} for $3MoS_2/G$ at a current density of 0.1 A g^{-1}. In the subsequent cycles, $1MoS_2/G$ and $2MoS_2/G$ electrode materials lost *ca.* 28 % of the initial capacity and the loss was *ca.* 20 % for $3MoS_2/G$ electrode. The irreversible capacity is due to the formation of solid electrolyte interphase (SEI) layer [76] and trapping of Li ions by high energy cites of electrode materials [32]. The first discharge curves of all electrode materials exhibited a small plateau around 1.8–1.9 eV (Fig. S3), which indicates an interaction of Li ions with elemental sulfur or S_2^{2-} pairs present at MoS_2 edges. The plateaus corresponding to the intercalation of Li ions between MoS_2 layers (around 1.1 V *vs.* Li/Li^+ [42]) and graphene layers (below 0.2 V *vs.* Li/Li^+ [4]), and the conversion of Li_xMoS_2 intercalates to Mo and LiS_2 (around 0.6 V *vs.* Li/Li^+ [42]) are difficult to distinguish on slopes, but should appear on CV curves. Such behavior is a characteristic of poorly ordered structures containing various adsorption sites [77].

To determine the potentials for electrochemical interaction of MoS_2/G with Li ions, we have measured CV curves at a scan rate of 0.1 mV s^{-1}. Typical curves for three initial full discharge-charge cycles are shown in Fig. 6a. Four prominent peaks at 1.58, 1.46, 0.2, and 0 V *vs.* Li/Li^+ are observed at the first insertion of Li ions into the electrode material. The first two peaks appear at the potentials, which are larger than the potential of Li_xMoS_2 intercalates formation. A study of MoS_3/graphene materials found the reduction peaks at 1.59 and 1.45 V, which were attributed to the interaction of MoS_3 with Li ions yielding MoS_2 and the subsequent intercalation of the obtained MoS_2, respectively [78]. Although these values are very close to the positions of the discussed peaks for our materials (Fig. 6a), we cannot use the above-mentioned assignment for the peak at 1.58 V because of the XRD, XPS, and HR TEM data indicated the formation of MoS_2 layers as the result of the synthesis. We suppose this peak is due to the insertion of Li ions into the interface between graphene and MoS_2. Indeed, the theory predicts that the accommodation of Li in MoS_2/graphene space should require more energy as compared to that between MoS_2 layers (~1.1 V) [79]. A wide CV peak centered at *ca.* 0.25 V can be attributed to the decomposition of Li_xMoS_2 into Mo and Li_2S. A sharp peak at *ca.* 0.01 V corresponds to the intercalation of Li ions between graphene layers. On the de-lithiation curve, there are two large peaks at 2.2 and 1.9 V and a weak peak at *ca.* 1.35 V that accompany the extraction of Li ions from the electrode materials. The latter peak can be due to the lithium de-intercalation through vacancy defects [77, 80] created in graphene layers under thermal shock conditions. The peaks with higher potentials correspond to

partial de-lithiation of lithium sulfides with the formation of Li_2S_n (n>4) and Li_2S_2, respectively [81]. The second and third CV curves showed a decrease in the areas of the reduction peaks at 1.46 and 0.25 V and rise of the peak at 1.58 V. These CV curves almost overlap, indicating the reversibility of reactions of the Li intercalation to MoS_2/graphene interface and redox interactions between sulfur and Li ions.

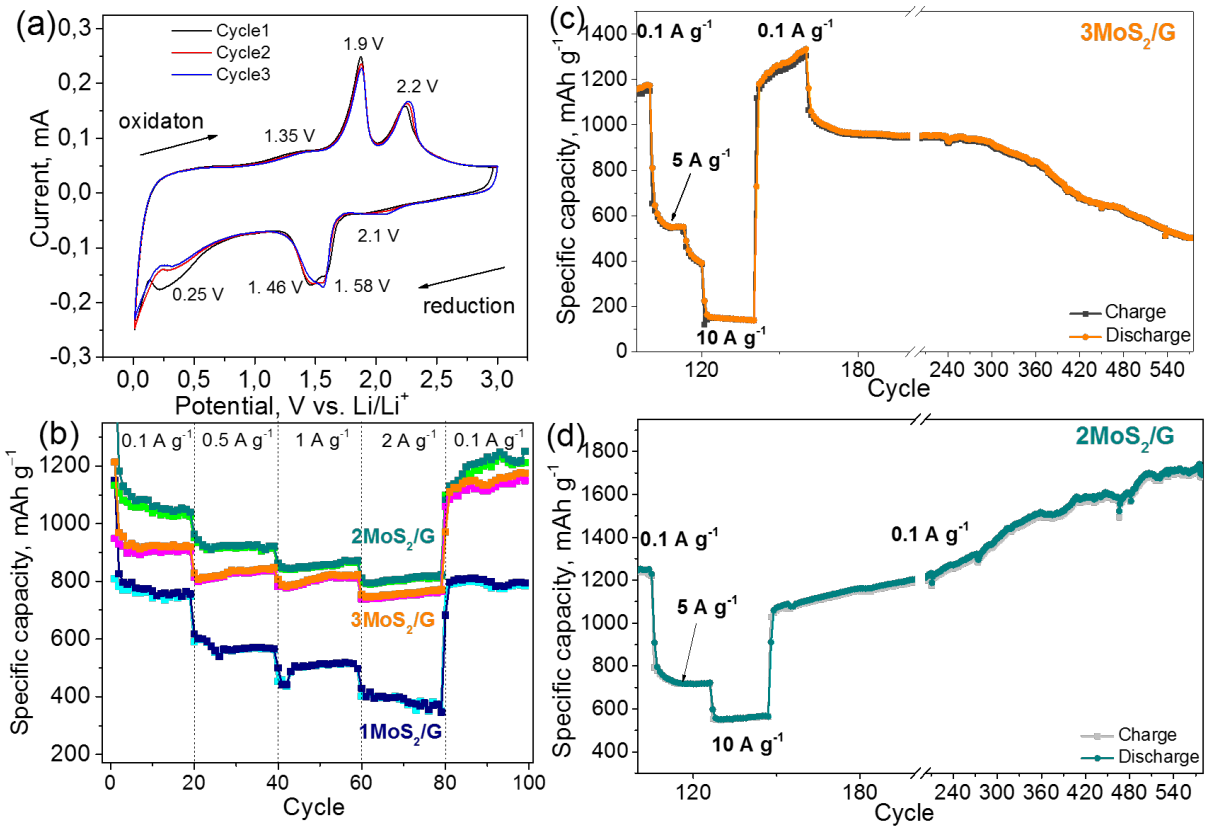

Figure 6. CV curves of $1MoS_2$/G for the first three cycles at a scan rate of 0.1 mV s^{-1} (a). Rate capability of synthesized materials (b). Consistent cycling of $3MoS_2$/G (c) and $2MoS_2$/G (d) at current densities of 5 A g^{-1}, 10 A g^{-1}, and 0.1 A g^{-1}.

Figure 6b compares the rate behavior of the electrode materials for ten cycles at different current densities. The best-performing material $2MoS_2$/G was able to reversibly deliver 1044, 924, 868, and 817 mAh g^{-1} at current densities of 0.1, 0.5, 1, and 2 A g^{-1}, respectively. The capacity of this electrode was even increased to 1246 mAh g^{-1}, when the current density was switched back to 0.1 A g^{-1} after 80 cycles. Material $3MoS_2$/G had the capacity values lower by 40–120 mAh g^{-1} than the corresponding values for $2MoS_2$/G. However, at a high current density of 2 A g^{-1} this electrode still delivered 769 mAh g^{-1} and its capacity reached 1165 mAh g^{-1} in the following cycles at 0.1 A g^{-1}. Material $1MoS_2$/G with the least MoS_2 loading showed the lowest values of the specific capacity at all applied current densities. The weight fraction of MoS_2 in this material is below 60 % (Table 1) and this may not be enough to provide a high capacity of the hybrid. For

further demonstration, we studied samples MoS_2 and G obtained from correspondently ATM and GO in thermal shock conditions (Fig. S4). At current densities of 0.1 and 0.5 A g^{-1}, pure MoS_2 had specific capacities comparable with the corresponding values for MoS_2/G materials, while the capacity dropped rapidly as the current density increased to 1 A g^{-1}. The Li-ion cell with thermally exfoliated graphene material worked stable at all current densities, but the capacity did not exceed 615 mAh g^{-1} at 0.1 A g^{-1}. These results confirm the benefits of combining the two components into hybrids.

The cells with two best hybrids were further tested at higher rates. The electrode $3MoS_2$/G sustained 548 mAh g^{-1} at a current density of 5 A g^{-1} and 140 mAh g^{-1} at 10 A g^{-1} (Fig. 6c). After twenty repeating discharge-charge cycles at 10 A g^{-1}, the current density was returned to 0.1 A g^{-1} that resulted in the growth of the specific capacity until 1327 mAh g^{-1}. However, after more than 150 successful operation cycles, the capacity dropped to 1060 mAh g^{-1} and then gradually decreased over the next four hundred cycles. The electrode $2MoS_2$/G delivered 717 and 564 mAh g^{-1} at current densities 5 and 10 A g^{-1}, respectively (Fig. 6d). The value of the specific capacity was 1060 mAh g^{-1} when the current density was decreased to 0.1 A g^{-1} and during the next 425 operation cycles the capacity stabilized around to 1730 mAh g^{-1}. The different behavior of $3MoS_2$/G and $2MoS_2$/G during long-term tests can be associated with different amounts of MoS_2 in the hybrid. An ultimate contact between graphene and MoS_2 surfaces is achieved when the weight ratio of MoS_2 to carbon is 1.45 [17]. An estimate from the CHNS data (Table 1) gives the values of *ca.* 1.35 for $2MoS_2$/G and *ca.* 2.48 for $3MoS_2$/G. Hence, the ratio of the components is close to optimal in the former hybrid, while MoS_2 overloads the latter material. The graphene component of $3MoS_2$/G cannot properly stabilize the redox-active component and provide sufficient electrical conductivity of the hybrid [46] whose capacity as a result decreases during cycling (Fig. 6c).

A gradual increase of the specific capacity under long-term repeated insertion/extraction of Li ions is uncommon phenomena for electrode materials but was previously observed for carbon materials [82], MoS_2 nanosheets on a Ti substrate [83], and MoS_2/carbon composites [36, 41, 48, 84, 85]. In the case of carbon, such behavior is attributed to the activation of initially closed pores [82, 48] and the extension of vacancies, which facilitate intercalation of Li ions between the layers [84]. A major contribution to the extra capacity in MoS_2 was related to the accommodation of several Li ions with Mo atoms and clusters [41]. Convincing identification of such species requires special approaches such as cryo-scanning TEM [40]. To find out the reasons for the increase in capacity in $2MoS_2$/G material, we analyzed discharge-charge curves measured at 540th cycle. Compared to initial battery operation (see the third cycle in Fig. S3), the discharge-charge curves have no distinguished plateaus at 540th cycle (Fig. S5). Hence, the electrode material is a mixture

of defective graphene-like layers, molybdenum clusters, and sulfur species. A gain in the capacity with long-term cycling was received from all reactions (Table S1), namely, the interaction of Li ions with carbon component below 0.2 V, Mo atoms and clusters between 0.2 and 1.9 V, and sulfur species above 1.9 V. During long repeating insertion/extraction of Li ions, the Mo nanoparticles formed during the MoS_2 conversion gradually decrease to atomic-scale and this creates more sites for the accommodation of lithium [41]. The interactions between Li ions and highly-dispersed molybdenum lead to an increase in the capacity of the material by about two times at compared to that at the third cycle (Table S1). At the same time, the contribution from the reaction of Li ions with graphene component increased by more than three times. HR TEM images observed vacancies in graphene layers (Fig. 5g). These vacancies can extend during the cycling [84] thus facilitating the insertion of more Li ions between the graphene layers. The ratio of the components in $2MoS_2/G$ allows part of the graphene surface to remain uncoated with MoS_2 and therefore the contribution from the defective carbon component in the capacity of this sample is so significant. A large amount of MoS_2 in $3MoS_2/G$ covers the entire surface of graphene (Fig. S6), blocking the access of Li ions to vacancies.

The rate tests show that the synthesized MoS_2/G materials can survive current densities of 5–10 A g^{-1} and recover initial capacity afterward. The specific capacities delivered by the $2MoS_2/G$ electrode are among the best values reported for MoS_2/carbon materials (Table 2). At the selected current densities of 0.1, 0.5, 5, and 10 A g^{-1} this electrode fails behind to only to two materials from the list, namely, the composite MoS_2/C-3, where curved and bent MoS_2 particles were distributed in an amorphous carbon matrix [37], and the sandwich-like structure from few-layered graphene and metallic 1T-MoS_2 nanosheets [41]. However, the syntheses of these materials are energy- and time-consuming, while our MoS_2/G materials are produced quickly and in a scalable manner.

Table 2. Comparison of the performance of $2MoS_2/G$ material in a lithium-ion battery with the best examples of high-rate MoS_2/carbon electrodes reported in the literature. Values exceeding capacities obtained in this work are highlighted in bold.

Sample	Reversible capacity (mAh g^{-1}) at given current density				Ref.
	0.1 A g^{-1}	0.5 A g^{-1}	5 A g^{-1}	10 A g^{-1}	
$2MoS_2/G$	1730	920	717	564	this work
VA-C/MoS_2	1085	891	702	-	11

EG-MoS_2	1385	1217	**970**	-	14
NDG/MoS_2	1050	810	460	-	19
HFMEC-91	954.5	-	675.7	562.9	20
MoS_2/GNS-15	1483	-	-	-	21
AC-MoS_2	1355	~1050	~830	670	23
MoS_2@NC	-	**1360**	565	-	24
MoS_2/hCNC	1535	**~1350**	633	543	25
MoS_2-NC	-	926	574	-	28
G/MoS_2	~1100	903	~640	-	29
MoS_2@C	~1180	~1080	~800	597	31
MoS_2/C-3	**1742.7**	**~1680**	-	**672.8**	37
1T-MoS_2/graphene	**1840**	~1130	~850	**750**	41
MoS_2/N-CNT	-	~1100	**~930**	**792**	75
MoS_3/r-GO	-	1276	**~1000**	-	76
1T-MoS_2/C	1150	900	680	600	86
MoS_2/GNRA-65.2wt%	-	854	~600	507	87
MoS_2/Mo_2N/C	958	775	575	-	88

The kinetics of charge storage in the synthesized MoS_2/G was studied from the analysis of CV curves measured at scan rates varied from 0.1 to 1 mV s^{-1} (Fig. 7a). The peak current (i) depends on the scan rate (v) according to the power law: $i=av^b$ [89]. A b value of 0.5 induces that diffusion controls an electrochemical process and for the case b=1 the process is capacitive. Figure 7b shows the plots log(i) *vs.* log(v) for the four main redox peaks observed in the CV curves (Fig. 7a). The b values determined from these plots are larger 0.85, hence capacitive-like processes dominate in the hybrids over diffusion-controlled reactions [90]. The largest impact of the diffusion is observed for the oxidation peak O2 (b=0.87). The equation $i(v)=k_1v + k_2v^{1/2}$ was used to quantify the capacitive (the first term) and diffusion (the second term) contributions at a certain scan rate [91].

The kinetics analysis carried out at 1 mV s^{-1} is presented in Fig. 7c, where the shaded region corresponds to the capacitive contribution. Figures 7d summarizes ratios of the capacitive and diffusion behaviors at the used scan rates. The capacitive contribution increases with the scan rate and this evidences that high-rate performance of the MoS_2/G materials is surface-controlled. A high degree of exfoliation of graphene and MoS_2 layers, the small lateral size of MoS_2, and tight contact between the components created in the conditions of thermal shock reaction provide the efficient exposure of the electrochemically active species to Li ions.

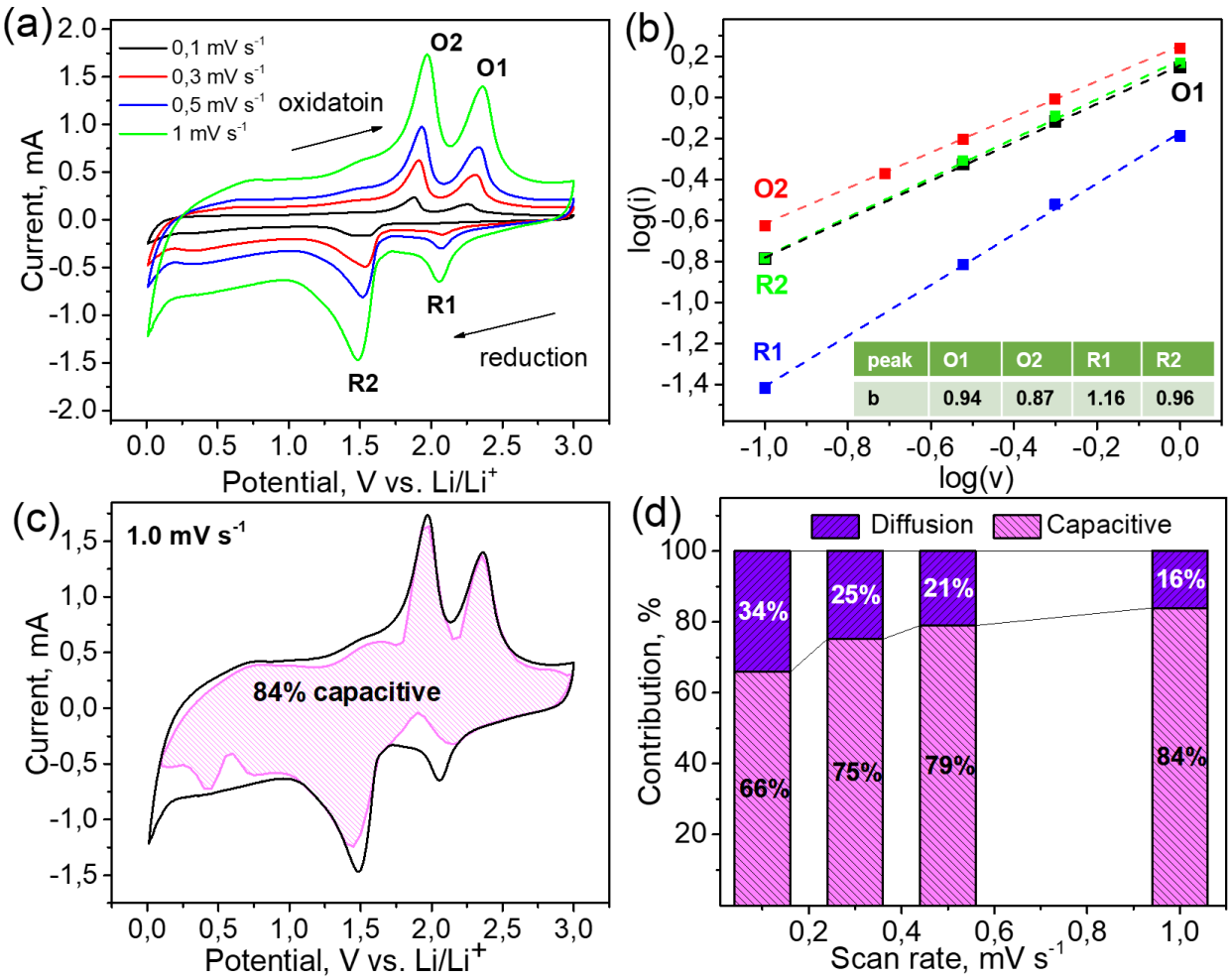

Figure 7. CV curves of MoS_2/G material at different scan rates (a), log(*i*) *vs.* log(*v*) plots for four redox peaks (b), contribution of the capacitive behavior into CV response measured at scan rate of 1 mV s^{-1} (c), the normalized ratio of capacitive and diffusion-controlled contributions at different scan rates (d).

4. Conclusions

MoS_2/graphene materials were synthesized in a simple way using GO and $(NH_4)_2MoS_4$, which are commercially available. GO easily exfoliates in water giving charged layers for the adsorption of $(NH_4)_2MoS_4$ species. Rapid freezing of the dispersion and sublimation of solvent leads to the formation of an aerogel with a fine distribution of the precursor compounds. Decomposition of the

aerogel in an inert atmosphere in the conditions of thermal shock produces defect-enriched graphene layers coupled with MoS_2 nanosheets perpendicular to or aligned along the graphene surface. The synthesis temperature of 400°C is sufficient for removal of most oxygen from GO and arrangement of Mo and S atoms in hexagonal MoS_2 lattices. High pressure created by the gases evolved during the synthesis, enables curving and intertwining of vertical MoS_2 nanosheets and formation of covalent bonding with graphene. As the result, obtained MoS_2/graphene materials possess a high capacity, high rate capability and stability in Li-ion batteries. The material with a ratio of MoS_2 to carbon of about 4 to 1 by the weight showed the best performance reversibly delivering 1044, 717, and 564 mAh g^{-1} at current densities of 0.1, 5, and 10 A g^{-1}. These values are among the best ones currently reported in the literature. Moreover, when the current density was switched from 10 to 0.1 A g^{-1} the specific capacity of the material increased to 1730 mAh g^{-1} during the next operation cycles. This phenomenon was related to the enlarging atomic vacancies in graphene layers, accommodation of several Li atoms around on a Mo atom, and complete extraction of Li ions from lithium sulfides. The last two processes are attributed to anchored and dispersed molybdenum and sulfur species on and between defective graphene layers.

Acknowledgments

The work was financially supported by the Russian Science Foundation (Grant 16-13-00016). The XPS measurements were conducted under support of the bilateral Program "Russian-German Laboratory at BESSY II". V.O.K. acknowledges financial support by the Spanish Ministry of Economy and Competitiveness (MINECO) within the Maria de Maeztu Units of Excellence Programme – MDM-2016-0618.

Declaration of Interest

None.

References

[1] Y. Jiao, A.M. Hafez, D. Cao, A. Mukhopadhyay, Y. Ma, H. Zhu, Metallic MoS_2 for high performance energy storage and energy conversion. Small 14 (2018) 1800640.

[2] T. Stephenson, Z. Li, B. Olsen, D. Mitin, Lithium ion battery applications of molybdenum disulfide (MoS_2) nanocomposites. Energy Environ. Sci. 7 (2014) 209–231.

[3] Y. Tan, C. Cheng, L. Zhang, Y. Li, J. Lu, Deciphering the reaction mechanism of lithium–sulfur batteries by in situ/operando synchrotron–based characterization techniques. Adv. Energy Mater. 9 (2019) 1900148.

[4] N. Nitta, F. Wu, J.T. Lee, G. Yushin, Li–ion battery materials: present and future. Materials Today 18 (2015) 252–264.

[5] A.P. Tiwari, H. Yoo, J.T. Lee, D. Kim, J.H. Park, H. Lee, Prevention of sulfur diffusion using MoS_2–intercalated 3D–nanostructured graphite for high–performance lithium–ion batteries. Nanoscale 7 (2015) 11928–11933.

[6] Y. Zhu, W. Peng, Y. Li, G. Zhang, F. Zhang, X. Fan, Multiple roles of a heterointerface in two–dimensional van der Waals heterostructures: insight into energy–related applications. J. Mater. Chem. A 7 (2019) 23577–23603.

[7] K. Chang and W. Chen, L–cysteine–assisted synthesis of layered MoS_2/graphene composites with excellent electrochemical performances for lithium ion batteries. ACS Nano 5 (2011) 4720–4728.

[8] K. Chang and W. Chen, In situ synthesis of MoS_2/graphene nanosheet composites with extraordinarily high electrochemical performance for lithium ion batteries. Chem. Commun. 47 (2011) 4252–4254.

[9] H. Wang, D. Tran, J. Qian, F. Ding, D. Losic , MoS_2/graphene composites as promising materials for energy storage and conversion applications. Adv. Mater. Interfaces 6 (2019) 1900915.

[10] Z. Yu, J. Ye, W. Chen, S. Xu, F. Huang, Fabrication of few–layer molybdenum disulfide/reduced graphene oxide hybrids with enhanced lithium storage performance through a supramolecule–mediated hydrothermal route. Carbon 114 (2017) 125–133.

[11] P. Zhang, Y. Liu, Y. Yan, Y. Yu, Q. Wang, M. Liu, High areal capacitance for lithium ions storage achieved by a hierarchical carbon/MoS_2 aerogel with vertically aligned pores. ACS Appl. Energy Mater. 1 (2018) 4814–4823.

[12] J. Guo, H. Zhu, Y. Sun, L. Tang, X. Zhang, Boosting the lithium storage performance of MoS_2 with graphene quantum dots. J. Mater. Chem. A 4 (2016) 4783–4789.

[13] V.H. Pham, K.-H. Kim, D.-W. Jung, K. Singh, E.-S. Oh, J.S. Chung, Liquid phase co–exfoliated MoS_2–graphene composites as anode materials for lithium ion batteries. J. Pow. Sources 244 (2013) 280–286.

[14] G. Wang, J. Zhang, S. Yang, F. Wang, X. Zhuang, K. Müllen, X. Feng, Vertically aligned MoS_2 nanosheets patterned on electrochemically exfoliated graphene for high-performance lithium and sodium storage. Adv. Energy Mater. 8 (2018) 1702254.

[15] D.H. Youn, C. Jo, J. Y. Kim, J. Lee, J. Sung, Lee, Ultrafast synthesis of MoS_2 or WS_2–reduced graphene oxide composites via hybrid microwave annealing for anode materials of lithium ion batteries. J. Pow. Sources 295 (2015) 228–234.

[16] S. G. Stolyarova, M. A. Kanygin, V. O. Koroteev, Y. V. Shubin, D. A. Smirnov, A.V. Okotrub, L. G. Bulusheva, High-pressure high-temperature synthesis of MoS_2/holey graphene hybrids and their performance in lithium-ion batteries. Phys. Status Solidi B 255 (2018) 1700262.

[17] S. G. Stolyarova, V. O. Koroteev, K. I. Baskakova, A. A. Makarova, A. V. Okotrub, L. G. Bulusheva, Anode materials from MoS_2 and multilayered holey graphene for Li-ion batteries. Fuller. Nanotubes Carbon Nanostruct. 28 (2020) 328–334.

[18] S. Wang, R. Wang, Q. Zhao, L. Ren, J. Wen, J. Chang et al, Freeze-drying induced self-assembly approach for scalable constructing MoS_2/graphene hybrid aerogels for lithium-ion batteries. J. Colloid Interface Sci. 544 (2019) 37–45.

[19] C. Zhao, X. Wang, J. Kong, J. M. Ang, P. S. Lee, Z. Liu, X. Lu, Self-assembly-induced alternately stacked single-layer MoS_2 and N-doped graphene: a novel van der Waals heterostructure for lithium-ion batteries. ACS Appl. Mater Interfaces 8 (2016) 2372–2379.

[20] Z. Sun, Y. Yao, J. Wang, X. Song, P. Zhang, L. Zhao, L. Gao, High rate lithium-ion batteries from hybrid hollow spheres with a few-layered MoS_2-entrapped carbon sheath synthesized by a space–confined reaction. J. Mater. Chem. A 4 (2016) 10425–10434.

[21] Y. Liu, Y. Zhao, L. Jiao, J. Chen, A graphene-like MoS_2/graphene nanocomposite as a high performance anode for lithium ion batteries. J. Mater. Chem. A 2 (2014) 13109–13115.

[22] M. Wang, Y. H. Xu, F. Lu, Z. Zhu, J. Y. Dong, D. L. Fang et al, Enhanced Li-ion-storage performance of MoS_2 through multistage structural design, ChemElectroChem 6 (2019) 1475–1484.

[23] J.-C. Seo, N. Umirov, S. B. Park, K. Lee, S.-S. Kim, Microalgae-derived hollow carbon-MoS_2 composite as anode for lithium–ion batteries. J. Industr. Engin. Chem. 79 (2019) 106–114.

[24] P. Guo, K. Sun, D. Liu, P. Cheng, M. Lv, Q. Liu, D. He, Molybdenum disulfide nanosheets embedded in hollow nitrogen-doped carbon spheres for efficient lithium/sodium storage with enhanced electrochemical kinetics. Electrochim. Acta 283 (2018) 646–654.

[25] M. Liu, H. Fan, O. Zhuo, X. Du, L. Yang, P. Wang et al, Vertically grown few-ayer MoS_2 nanosheets on hierarchical carbon nanocages for pseudocapacitive lithium storage with ultrahigh–rate capability and long-term recyclability. Chem. Eur. J 25 (2019) 3843–3848.

[26] W. Qi, J. G. Shapter, Q. Wu, T. Yin, G. Gao, D. Cui, Nanostructured anode materials for lithium–ion batteries: principle, recent progress and future perspectives. J. Mater. Chem. A 5 (2017) 19521–19540.

[27] Y. Lu, L. Yu, X.W. Lou, Nanostructured conversion-type anode materials for advanced lithium-ion batteries. Chem 4 (2018) 972–996.

[28] M. Zhen, J. Wang, S.-q. Guo, B. Shen, Vertically aligned nanosheets with MoS_2/N–doped–carbon interfaces enhance lithium–ion storage. Appl. Surf. Sci. 487 (2019) 285–294.

[29] H. Yu, C. Ma, B. Ge, Y. Chen, Z. Xu, C. Zhu et al, Three-dimensional hierarchical architectures constructed by graphene/MoS_2 nanoflake arrays and their rapid charging/discharging properties as lithium–ion battery anodes. Chem. Eur. J. 19 (2013) 5818–5823.

[30] L. Ma, J. Ye, W. Chen, D. Chen, J. Y. Lee, Gemini surfactant assisted hydrothermal synthesis of nanotile-like MoS_2/graphene hybrid with enhanced lithium storage performance. Nano Energy 10 (2014) 144–152.

[31] D. Sun, X. Miao, J. Yang, H. Li, X. Zhou, Z. Lei, MoS_2 nanosheets vertically aligned on hierarchically porous graphitic carbon for high–performance lithium storage. J. Electrochem. Soc. 165 (2018) A2859–A2865.

[32] L. G. Bulusheva, V. O. Koroteev, S. G. Stolyarova, A. L. Chuvilin, P. E. Plyusnin, Yu. V. Shubin et al, Effect of in–plane size of MoS_2 nanoparticles grown over multilayer graphene on the electrochemical performance of anodes in Li-ion batteries. Electrochim. Acta 283 (2018) 45–53.

[33] J.-M. Jeong, K. G. Lee, S.-J. Chang, J. W. Kim, Y.-K. Han, S. J. Lee, B. G. Choi, Ultrathin sandwich-like MoS_2@N-doped carbon nanosheets for anodes of lithium ion batteries. Nanoscale 7 (2015) 324–329.

[34] Y. Jing, E. O. Ortiz-Quiles, C. R. Cabrera, Z. Chen, Z. Zhou, Layer-by-layer hybrids of MoS_2 and reduced graphene oxide for lithium ion batteries. Electrochim. Acta 147 (2014) 392–400.

[35] Z. Wang, T. Chen, W. Chen, K. Chang, L. Ma, G. Huang et al, CTAB-assisted synthesis of single-layer MoS_2-graphene composites as anode materials pf Li-ion batteries. J. Mater. Chem. A 1 (2013) 2202–2210.

[36] Z. Wu, W. Lei, J. Wang, R. Liu, K. Xia, C. Xuan, D. Wang, Various structured molybdenum-based nanomaterials as advanced anode materials for lithium ion batteries. ACS Appl. Mater. Interfaces 9 (2017) 12366–12372.

[37] G.-H. Lee, S.-J. Kim, M.-C. Kim, H.-S. Choe, D.-M. Kim, S.-B. Han et al, In situ formation of MoS_2/C nanocomposite as an anode for high-performance lithium–ion batteries. RCS Adv. 6 (2016) 92259–92266.

[38] H. Wang, D. Ren, Z. Zhu, P. Saha, H. Jiang, C. Li, Few-layer MoS_2 nanosheets incorporated into hierarchical porous carbon for lithium–ion batteries. Chem. Eng. J. 288 (2016) 179–184.

[39] Z. Zhu, S. Xi, L. Miao, Y. Tang, Y. Zeng, H. Xia et al, Unraveling the formation of amorphous MoS_2 nanograins during the electrochemical delithation process. Adv. Funct. Mater. 29 (2019) 1904843.

[40] S.-H. Yu, M. J. Zachman, K. Kang, H. Gao, X. Huang, F. J. DiSalvo et al, Atomic–scale visualization of electrochemical lithiation processes in monolayer MoS_2 by cryogenic electron microscopy, Adv. Energy Mater. 9 (2019) 1902773.

[41] L. Wang, Q. Zhang, J. Zhu, X. Duan, Z. Xu, Y. Liu et al, Nature of extra capacity in MoS_2 electrodes: Molybdenum atoms accomodate with lithium. Energy Storage Mater. 16 (2019) 37–45.

[42] R. Zhang, Y. Qin, P. Liu, C. Jia, Y. Tang, H. Wang, How does molybdenum disulfide store charge: A minireview. ChemSusChem 13 (2020) 1–13.

[43] L. Zhang, D. Sun, J. Kang, J. Feng, H. A. Bechtel, L.–W. Wang et al, Electrochemical reaction mechanism of the MoS_2 electrode in a lithium-ion cell revealed by in situ and operando X–ray absorption spectroscopy. Nano Lett. 18 (2018) 1466–1475.

[44] S. Xia, Y. Wang, Y. Liu, C. Wu, M. Wu, H. Zhang, Untrathin MoS_2 nanosheets tightly anchoring onto nitrogen-doped graphene for enhanced lithium storage properties. Chem. Eng. J. 332 (2018) 431–439.

[45] E. G. da Silveira Firmiano, A. C. Rabelo, C. J. Dalmaschio, A. N. Pinheiro, E. C. Pereira, W. H. Schreiner, E. R. Leite, Supercapacitor electrodes obtained by directly bonding 2D MoS_2 on reduced graphene oxide. Adv. Energy. Mater. 4 (2014) 1301380.

[46] M. Han, Z. Lin, J. Yu. Ultrathin MoS_2 nanosheets homogenously embedded in a N,O-codoped carbon matrix for high-performance lithium and sodium storage. J Mater. Chem. A 7 (2019) 4804–4812.

[47] V. O. Koroteev, L. G. Bulusheva, A. V. Okotrub, N. F. Yudanov, D. V. Vyalikh, Formation of MoS_2 nanoparticles on the surface of reduced graphite oxide. Phys. Status Solidi B 248 (2011) 2740–2743.

[48] S. G. Stolyarova, V. O. Koroteev, Yu. V. Shubin, P. E. Plyusnin, A. A. Makarova, A. V. Okotrub, L. G. Bulusheva, Pressure-assisted interface engineering in MoS_2/holey graphene hybrids for improved performance in Li-ion batteries. Energy Technol. 7 (2019) 1900659.

[49] M. Cai, D. Thorpe, D. H. Adamson, H. C. Schniepp, Methods of graphite exfoliation. J. Mater. Chem. 22 (2012) 24992–25002.

[50] S. G. Stolyarova, E. S. Kobeleva, I. P. Asanov, A. V. Okotrub, L. G. Bulusheva, Effect of the graphite oxide composition on the structure of products obtained by sulfuric acid treatment at elevated temperatures. J. Struct. Chem. 58 (2017) 1180–1186.

[51] V. V. Neklyudov, N. R. Khafizov, I. A. Sedov, A. M. Dimiev, New insights into the solubility of graphene oxide in water and alcohols. Phys. Chem. Chem. Phys. 19 (2017) 17000–17008.

[52] A. M. Dimiev, L. B. Alemany, J. M. Tour, Graphene oxide. Origin of acidity, its instability in water, and a new dynamic structural model. ACS Nano 7 (2013) 576–588.

[53] H. W. Wang, P. Skeldon, G. E. Thompson, G. C. Wood, Synthesis and characterization of molybdenum disulphide formed from ammonium tetrathiomolybdate. J. Mater. Sci. 32 (1997) 497–502.

[54] L. Sygellou, An in–situ photoelectron spectroscopy study of the thermal processing of ammonium tetrathiomolybdate, $(NH_4)_2MoS_4$, precursor. Appl. Surf. Sci. 476 (2019) 1079–1085.

[55] S. Pei, H.-M. Cheng, The reduction of graphene oxide. Carbon 50 (1012) 3210–3228.

[56] Y. Xu, K. Sheng, C. Li, G. Shi , Self-assembled graphene hydrogel via a one-step hydrothermal process. ACS Nano 4 (2010) 4324–4330.

[57] W. Xu, S. Li, S. Zhou, J. K. Lee, S. Wang, S. G. Sar et al, Large dendritic monolayer MoS_2 grown by atmospheric pressure chemical vapor deposition for electrocatalysis. ACS Appl. Mater. Interfaces 10 (2018) 4630–4639.

[58] A. K. Budumuru, B. Rakesh, C. Sudakar, Enhanced high rate capability of Li intercalation in planar and edge defect–rich MoS_2 nanosheets. Nanoscale 11 (2019) 8882–8897.

[59] S. Wang, B.Y. Guan, L. Yu, X.W. Lou, Rational design of three-layered TiO_2@carbon@MoS_2 hierarchical nanotubes for enhanced lithium storage. Adv. Mater. 29 (2017) 1702724.

[60] H. Li, Q. Zhang, C. C. R. Yap, B. K. Tay, T. H. T. Edwin, A. Olivier, D. Baillargeat, From bulk to monolayer MoS_2: Evolution of Raman scattering. Adv. Funct. Mater. 22 (2012) 1385–1390.

[61] C. Lee, H. Yan, L. E. Brus, T. F. Heinz, J. Hone, S. Ryu, Anomalous lattice vibrations of single- and few-layer MoS_2. ACS Nano 4 (2010) 2695–2700.

[62] X. Zhang, R. Zhang, X. Zheng, Y. Zhang, X. Zhang, C. Deng et al, Interlayer difference of bilayer-stacked MoS_2 structure: Probing by photoluminescence and Raman spectroscopy. Nanomater. 9 (2019) 796.

[63] M. S. Dresselhaus, A. Jorio, M. Hofmann, G. Dresselhaus, R. Saito, Perspectives on carbon nanotubes and graphene Raman spectroscopy. Nano Lett. 10 (2010) 751–758.

[64] D. F. Báez, H. Pardo, I. Laborda, J. F. Marco, C. Yáñez, S. Bollo, Reduced graphene oxides : Influence of the reduction method on the electrocatalytic effect towards nucleic acid oxidation. Nanomater. 7 (2017) 168.

[65] V. A. Tur, A. V. Okotrub, M. M. Shmakov, E. O. Fedorovskaya, I. P. Asanov, L. G. Bulusheva, Functional composition and supercapacitor properties of graphite oxide reduced with hot sulfuric acid. Phys. Status Solidi B 250 (2013) 2747–2752.

[66] H. L. Poh, P. Simek, Z. Sofer, M. Pumera, Sulfur-doped graphene via thermal exfoliation of graphite oxide in H_2S, SO_2, or CS_2 gas. ACS Nano 7 (2013) 5262–5272.

[67] J. Gao, J. He, N. Wang, X. Li, Z. Yang, K. Wang et al, Robust C-S bond integrated graphdiyne-MoS_2 nanohybrids for enhanced lithium storage capability. Chem. Eng. J. 373 (2019) 660–667.

[68] V. O. Koroteev, D. A. Bulushev, A. L. Chuvilin, A. V. Okotrub, L. G. Bulusheva, Nanometer-sized MoS_2 clusters on graphene flakes for catalytic formic acid decomposition. ACS Catal. T (2014) 3950–3956.

[69] O. V. Sedelnikova, O. A. Gurova, A. A. Makarova, A. D. Fedorenko, A. D. Nikolenko, P. E. Plyusnin et al, Light-induced sulfur transport inside single–walled carbon nanotubes. Nanomater. 10 (2020) 818.

[70] M. Huang, H. Chen, J. He, B. An, L. Sun, Y. Li et al, Ultra small few layer MoS_2 embedded into three-dimensional macro-micro-mesoporous carbon as a high performance

lithium ion batteries anode with superior lithium storage capacity. Electrochim. Acta 317 (2019) 638–647.

[71] H. G. Sanchez Casalongue, J. D. Benck, C. Tsai, R. K. B. Karlsson, S. Kaya, M. L. Ng, L. G. M. Pettersson, F. Abild-Pedersen, J. K. Norskov, H. Ogasawara, T. F. Jaramillo, A. Nilsson, Operando characterization of an amorphous molybdenum sulfide nanoparticle catalyst during the hydrogen evolution reaction. J. Phys. Chem. C 118 (2014) 29252–29259.

[72] A. Bruix, H. G. Fűchtbauer, A. K. Tuxen, A. S. Walton, M. Andersen, S. Porsgaard, F. Besenbacher, B. Hammer, J. V. Lauritsen, In situ detection of active edge sites in single-layer MoS_2 catalysts. ACS Nano 9 (2015) 9322–9330.

[73] A.-L. Hamon, J. Verbeeck, D. Schryvers, J. Benedikt, R. M. C. M. v. d. Sanden, ELNES study of carbon K–edge spectra of plasma deposited carbon films. J. Mater. Chem. 14 (2004) 2030–2035.

[74] T. Wang, G. Zhao, C. Sun, L. Zhang, Y. Wu, X. Hao, Y. Shao, Graphene–assisted exfoliation of molybdenum disulfide to fabricate 2D heterostructure for enhancing lithium storage. Adv. Mater. Interfaces 4 (2017) 1601187.

[75] T. Wu, M. Jing, Y. Liu, X. Ji, Binding low crystalline MoS_2 nanoflakes on nitrogen-doped carbon nanotube: towards high–rate lithium and sodium storage. J. Mater. Chem. A 7 (2019) 6439–6449.

[76] S. J. An, J. Li, C. Daniel, D. Mohanty, S. Nagpure, D. L. Wood III, The state of understanding of the lithium–ion–battery graphite solid electrolyte interphase (SEI) and its relationship to formation cycles. Carbon 105 (2016) 52–76.

[77] L. G. Bulusheva, S. G. Stolyarova, A. L. Chuvilin, Yu. V. Shubin, I. P. Asanov, A. M. Sorokin et al, Creation of nanosized holes in graphene planes for improvement of rate capability of lithium–ion batteries. Nanotechnology 29 (2018) 134001.

[78] U. Chang, J. T. Lee, J.–M. Yun, B. Lee, S. W. Lee, H.–I. Joh et al, In situ self-formed nanosheet MoS_3/reduced graphene oxide material showing superior performance as a lithium–ion battery cathode.ACS Nano 13 (2019) 1490–1498.

[79] H. Jiang, D. Ren, H. Wang, Y. Hu, S. Guo, H. Yuan et al, 2D monolayer MoS_2-carbon interoverlapped superstructure: Engineering ideal atomic interface for lithium ion storage. Adv. Mater. 27 (2015) 3687–3695.

[80] S. G. Stolyarova, A. V. Okotrub, Yu. V. Shubin, I. P. Asanov, A. A. Galitsky, L. G. Bulusheva, Effect of hot pressing on the electrochemical performance of multilayer holey graphene materials in Li-ion batteries. Phys. Status Solidi B 255 (2018) 1800202.

[81] U. K. Sen, P. Johari, S. Basu, C. Nayak, S. Mitra, An experimental and computational study to understand the lithium storage mechanism in molybdenum disulfide, Nanoscale 6 (2014) 10243–10254.

[82] J. Bai, B. Zhao, J. Zhou, J. Si, Z. Fang, K. Li et al, Glucose-induced synthesis of 1T-MoS_2/C hybrid for high-rate lithium-ion batteries. Small 15 (2019) 1805420.

[83] Y. Liu, X. Wang, X. Song, Y. Dong, L. Yang, L. Wang et al, Interlayer expanded MoS_2 enabled by edge effect of graphene nanoribbons for high performance lithium and sodium ion batteries. Carbon 109 (2016) 461–471.

[84] K. Chang, D. Geng, X. Li, J. Yang, Y. Tang, M. Cai et al, Ultrathin MoS_2/nitrogen–doped graphene nanosheets with highly reversible lithium storage. Adv. Energy Mater. 3 (2013) 839–844.

[85] S. B. Patil, K. Adpakpang, S. M. Oh, J. M. Lee, S.-J. Hwang, Reductive hybridization route with exfoliated graphene oxide and MoS_2 nanosheets to efficient electrode materials, Electrochim. Acta 176 (2015) 188–196.

[86] J. Bai, B. Zhao, J. Zhou, J. Si, Z. Fang, K. Li et al, Glucose-induced synthesis of 1T-MoS_2/C hybrid for high-rate lithium-ion batteries. Small 15 (2019) 1805420.

[87] Y. Liu, X. Wang, X. Song, Y. Dong, L. Yang, L. Wang et al, Interlayer expanded MoS_2 enabled by edge effect of graphene nanoribbons for high performance lithium and sodium ion batteries. Carbon 109 (2016) 461–471.

[88] S. Yang, Y. Zhang, S. Wang, J. Shi, X. Liu, L. Li, Rational construction of MoS_2/Mo_2N/C hierarchical porous tubular nanostructres for enhanced lithium storage. J. Mater. Chem. A 7 (2019) 23886–23894.

[89] H. Lindsröm, S. Södergren, A. Solbrand, H. Rensmo, J. Hjelm, A. Hagfeldt, S.-E. Lindquist, Li^+ ion insertion in TiO_2 (anatase). 2. Voltammetry on nanoporous films. J. Phys. Chem. B 101 (1997) 7717–7722.

[90] T. S. Mathis, N. Kurra, X. Wang, D. Pinto, P. Simon, Y. Gogotsi, Energy storage data reporting in perspective-guidelines for interpreting the performance of electrochemical energy storage systems. Adv. Energy Mater. 9 (2019) 1902007.

[91] T. Wang, Z. Xu, J. Yang, X. Liu, Y. Cheng, J. Li et al, Tailoring MoS_2 ultrathin sheets anchored on graphene flexible supports for superstable lithium-ion battery anodes. Part. Part. Syst. Charact. 36 (2019) 1900197.